NANO LETTERS

pubs.acs.org/NanoLett Letter

Steering Three-Dimensional Li_2S Deposition via a Janus-Structured Separator with a Dual-Ion/Electron-Conducting Interfacial Mediator for Low-Temperature Lithium−Sulfur Batteries

Wen Yan, Xiaoyue Li, Peng Liu, Chi Wang, Hanpei Liu, Chao Lai,* and Zhong Jin*

Cite This: https://doi.org/10.1021/acs.nanolett.6c00616 Read Online

ACCESS | Metrics & More | Article Recommendations | Supporting Information

ABSTRACT: Lithium−sulfur (Li-S) batteries face critical challenges from sluggish sulfur redox kinetics, polysulfide shuttle, and lithium dendrite growth. Herein, a Janus-structured separator featuring a miscible polystyrene/poly(methyl methacrylate) (PSA) gel buffer layer and a cathode-facing single-layer coating of ordered mesoporous carbon (s-OMC) is prepared as both charge-carrier transport vehicle and electron transfer mediator. The PSA layer endows dendrite-free lithium deposition and physically isolates the conductive s-OMC from the anode to prevent short circuits. Meanwhile, s-OMC with parallel aligned nanochannels enhances Li^+ diffusivity and supplies abundant electrons to steer controlled three-dimensional Li_2S deposition. This dual-functional architecture effectively mitigates interfacial passivation and accelerates sulfur redox kinetics. Consequently, Li-S batteries based on the Janus-structured PP/PSA/s-OMC separator deliver exceptional electrochemical performances under practical conditions, including stable cycling at a high sulfur loading (5.3 mg cm^{-2} or 5.43 mAh cm^{-2}), outstanding rate capability (704 mAh g^{-1} at 5 C), and remarkable low-temperature operation (922 mAh g^{-1} at −20 °C).

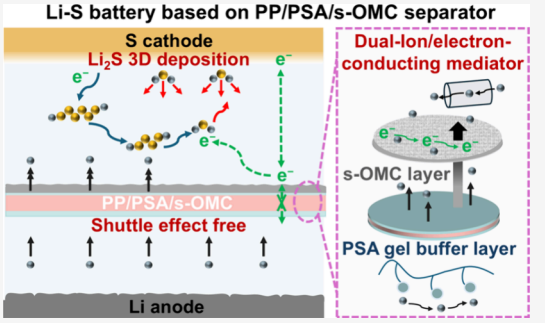

KEYWORDS: *Lithium−sulfur batteries, Janus-structured separator, Ordered mesoporous carbon, Three-dimensional Li_2S deposition, Low-temperature tolerance*

Downloaded via NANJING UNIV on April 15, 2026 at 03:16:36 (UTC).
See https://pubs.acs.org/sharingguidelines for options on how to legitimately share published articles.

Lithium-sulfur (Li-S) batteries are regarded as a promising next-generation energy storage technology due to sulfur's exceptional theoretical capacity (1675 mAh g^{-1}), natural abundance, low cost, and environmental benignity.[1−4] However, their practical application faces significant challenges, including the insulating nature of sulfur/lithium sulfide (Li_2S), sluggish sulfur redox kinetics, polysulfides (LiPSs) shuttle, and lithium dendrite growth.[5,6] To address these issues, numerous efforts have been dedicated to sulfur cathode engineering,[7−10] separator modification,[11−14] lithium anode protection,[15−17] and novel electrolyte design.[18−20] Among these strategies, separator modification has emerged as a particularly effective strategy. By optimization of interfacial reaction kinetics, functional interlayers introduced via separator modification enable higher sulfur loadings and improved capacity utilization toward practical high-energy-density Li-S batteries. Furthermore, these interlayers are less susceptible to passivation by Li_2S/Li_2S_2 discharge products during cycling.[21,22]

Separator modification approaches in Li-S batteries typically incorporate cathode-facing coatings of carbonaceous materials,[23−25] inorganic compounds,[13,26] functional polymers,[27] or their composites.[14,28] These interlayers primarily function as physical barriers or adsorption/catalytic sites to mitigate polysulfide shuttling and accelerate electrochemical kinetics. To achieve excellent battery performance, optimizing the conversion of soluble LiPSs to solid Li_2S is especially critical, as this rate-limiting step governs 75% of the theoretical capacity. During discharge, LiPS species accumulate at the cathode-separator interface and migrate toward the lithium anode side via concentration gradients, causing active material loss and capacity fading. Moreover, the insulating Li_2S discharge product passivates the electrode and catalyst surfaces, severely impeding subsequent reaction kinetics. For Li-S batteries under harsh operating conditions such as low temperature, high sulfur loading, and lean electrolyte, the sluggish deposition of Li_2S exacerbates interfacial passivation, leading to precipitous decline of capacity utilization and reduced cycling stability.[29,30] Therefore, promoting efficient LiPSs-to-Li_2S conversion is paramount in the design of separator modification approaches. While carbonaceous materials (e.g., carbon nanotubes, graphene, and carbon spheres) are widely

Received: February 5, 2026
Revised: March 31, 2026
Accepted: March 31, 2026

ACS Publications © XXXX American Chemical Society

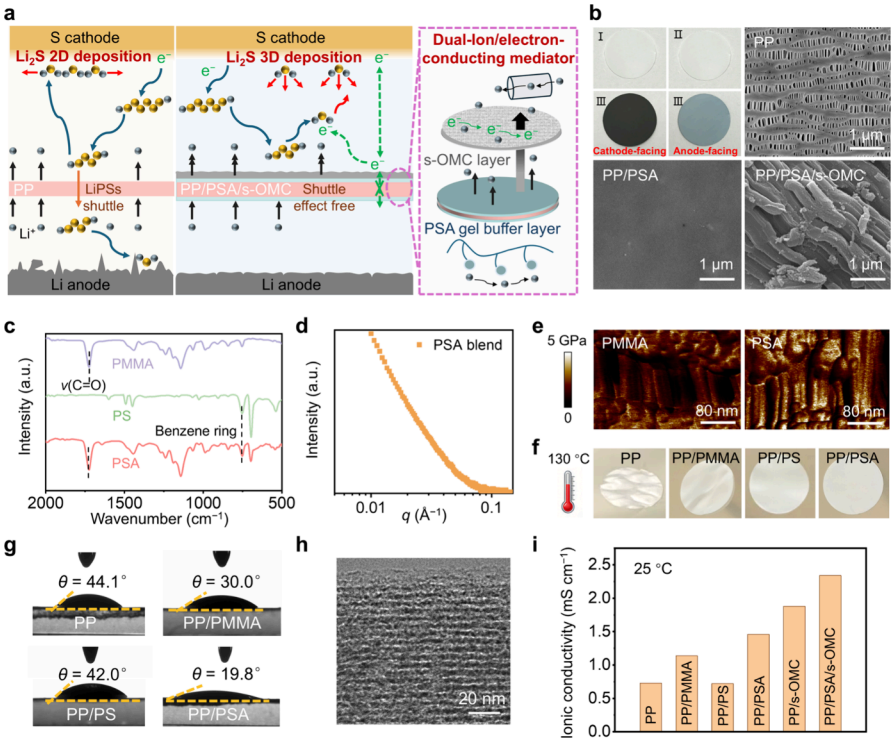

Figure 1. (a) Schematic illustrating the structure of the Janus-structured PP/PSA/s-OMC separator and its roles as a charge-carrier transport vehicle and electron transfer mediator to induce 3D Li_2S deposition at the interface. (b) Digital photographs and SEM images of different separators. I: PP, II: PP/PSA and III: PP/PSA/s-OMC. (c) FTIR spectra comparing pristine PMMA, PS, and the blended PSA. (d) SAXS plot of PSA blend. (e) AFM modulus mappings of PMMA and PSA. (f) Thermal stability tests at 130 °C. (g) Contact angle measurements quantifying electrolyte wettability of separators. (h) HRTEM image of s-OMC. (i) Ionic conductivity tests of different separators.

used in interlayers, they are primarily investigated as physical barriers or conductive scaffolds for catalysts; however, their intrinsic roles in regulating reaction kinetics at the electrolyte/electrode interface, particularly the deposition mode of Li_2S, have rarely been explored.

Herein, we design a Janus-structured separator as both a charge-carrier transport vehicle and electron transfer mediator, directionally steering Li_2S deposition into three-dimensional (3D) pathways at the interface. Our strategy integrates a miscible blend of polystyrene (PS) and poly(methyl methacrylate) (PMMA), denoted as PSA, as an encapsulation layer on the polypropylene (PP) separator. This PSA layer serves dual roles: (i) reducing interfacial impedance to enable dendrite-free lithium plating/stripping and (ii) acting as a gel polymer buffer to prevent internal short circuits by isolating subsequent conductive coatings from the lithium anode. Furthermore, a cathode-facing single layer of ordered mesoporous carbon (s-OMC) was applied as a model carbonaceous material. The s-OMC interfacial layer functions as a dual-ion/electron-conducting interfacial mediator, synergistically enhancing Li^+ diffusivity through parallel-aligned nanochannels and promoting spatially controlled 3D nucleation and growth of Li_2S by supplying abundant electrons and activating sulfur species at the interface (Figure 1a). This deposition mode effectively mitigates electrode passivation and accelerates sulfur conversion kinetics. The Janus PP/PSA/s-OMC separator delivers exceptional Li-S battery performances under challenging conditions: stable cycling at high sulfur loading (5.3 mg cm^{-2}), high rate (5 C), and low temperature of −20 °C.

PP separators are widely used in Li-S batteries due to their chemical stability and low cost. However, their inherently large pore size (>100 nm, Figure 1b) fosters LiPS shuttling, leading to active material depletion and lithium anode corrosion. Moreover, the unsuitable pore size distribution and insufficient electrolyte wettability of conventional PP separators cause uneven Li^+ plating and lithium dendrite growth. PMMA has been considered as a modifying layer due to its polar ester groups and amorphous nature, which exhibits strong electrolyte affinity and high ionic conductivity.[31] However, its poor mechanical strength compromises the structural stability of the separators. To overcome this constraint, PS with a rigid benzene structure is introduced to form a miscible PS−PMMA (PSA) blend. Fourier transform infrared spectra (FTIR) show characteristic bands at 1730 cm^{-1} (C═O stretching in PMMA) and 754 cm^{-1} (monosubstituted benzene ring bending from PS) in the PSA blend and PP/PSA separator (Figure 1c, Figure S1), indicating the successful incorporation of polymer coating. Small-angle X-ray scattering (SAXS) analysis shows a monotonic decrease in the scattering intensity without characteristic peaks (Figure 1d), demonstrating a homogeneously miscible PSA phase. Atomic force microscopy (AFM) analysis exhibits an enhanced Young's modulus for PSA compared to pure PMMA (Figure 1e), confirming improved mechanical robustness through PS incorporation. Thermal stability tests at 130 °C show that the PP separator shrinks significantly, while PP/PMMA exhibits slight deformation (Figure 1f). In comparison, both PP/PS and PP/PSA maintain dimensional integrity. Thermogravimetric analysis (TGA) further indicates that PMMA begins to decompose

https://doi.org/10.1021/acs.nanolett.6c00616
Nano Lett. XXXX, XXX, XXX−XXX

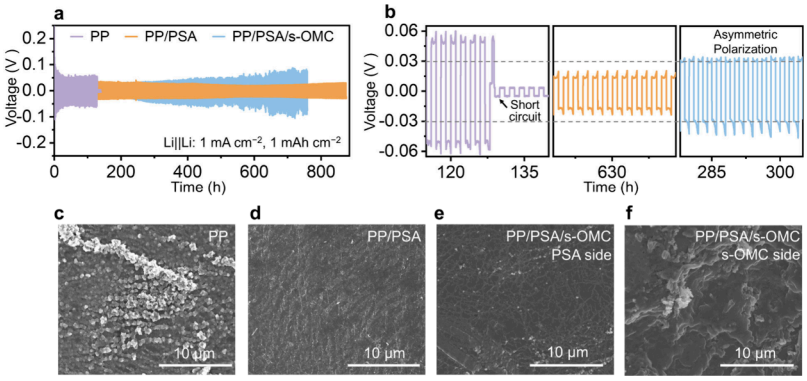

Figure 2. (a) Voltage profiles of Li||Li symmetric cells cycled at a current density of 1 mA cm^{-2} and plating capacity of 1 mAh cm^{-2} using PP, PP/PSA, and PP/PSA/s-OMC separators. (b) Magnified voltage hysteresis regions. (c-f) SEM images of the cycled Li foils after 50 cycles.

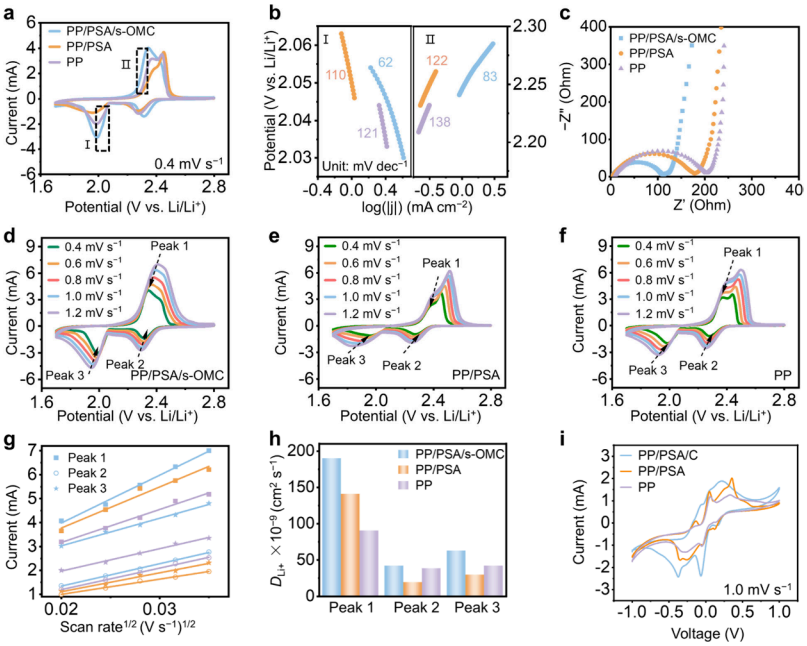

Figure 3. (a) CV curves of Li-S batteries at a scan rate of 0.4 mV s^{-1}. (b) Tafel slopes of the reduction peak (I) and oxidation peak (II). (c) Nyquist plots of Li-S batteries. (d-f) CV curves at different scan rates from 0.4 to 1.2 mV s^{-1}. (g) Relationship between the peak currents in the CV curves and the square root of the scan rates. (h) Apparent Li^+ ion diffusion coefficient (D_{Li^+}) values obtained from CV. (i) CV curves of Li_2S_6 symmetric cells at a scan rate of 1.0 mV s^{-1}.

around 100 °C, whereas PS and the PSA blend demonstrate improved thermal stability (Figure S2).

Contact angle measurements show enhanced electrolyte wettability after the surface modification of the gel layer (Figure 1g). Pure PP separator, composed of nonpolar alkane chains, has poor affinity for electrolytes (contact angle of 44.1°). PP/PMMA shows a reduced contact angle of 30.0° owing to the polar ester groups in PMMA. Notably, the PP/PSA separator achieves the best lyophilic property (contact angle of 19.8°), suggesting that the homogeneous blending of PS and PMMA may expose or arrange polar ester groups more effectively. Benefiting from favorable Li^+ interaction and improved wettability, PP/PSA achieves higher ionic conductivity (1.46 mS cm^{-1}) than PP (0.73 mS cm^{-1}) (Figure S3, Table S1). SEM images reveal that the PSA gel infiltrates into the pores of the PP separator (Figure 1b, Figure S4), resulting in a compositionally and mechanically uniform buffer layer that eliminates voids at the interface of the PP/PSA separator. By removing these voids, the gel layer homogenizes the electric field and acts as a physical barrier to prevent internal short circuits.

To further optimize ion transport, the s-OMC layer was selectively applied to the cathode-facing side of the PP/PSA separator (Figure 1b, Figure S5). Upon optimizing the coating thickness, the 6 μm s-OMC layer was identified as optimal in balancing structural integrity and electrochemical performance (Figures S6, S7). Uniform mesopores (5.6 nm) in the s-OMC create parallel-aligned nanochannels that minimize ion transport tortuosity and shorten the ion diffusion path (Figure 1h, Figure S8). The high specific surface area (882.2 m^2 g^{-1}) of s-OMC provides abundant adsorption sites for ions and solvents, thus establishing continuous ion-conduction pathways. Furthermore, the optimized mesopore size matches the solvation sheath dimensions of Li^+ ions, enabling partial desolvation and lowering the activation energy for ion migration.[32] Consequently, the PP/PSA/s-OMC exhibits a high ionic conductivity of 2.34 mS cm^{-1} (Figure 1i). The X-ray diffraction (XRD) pattern of s-OMC shows a sharp peak at

https://doi.org/10.1021/acs.nanolett.6c00616
Nano Lett. XXXX, XXX, XXX−XXX

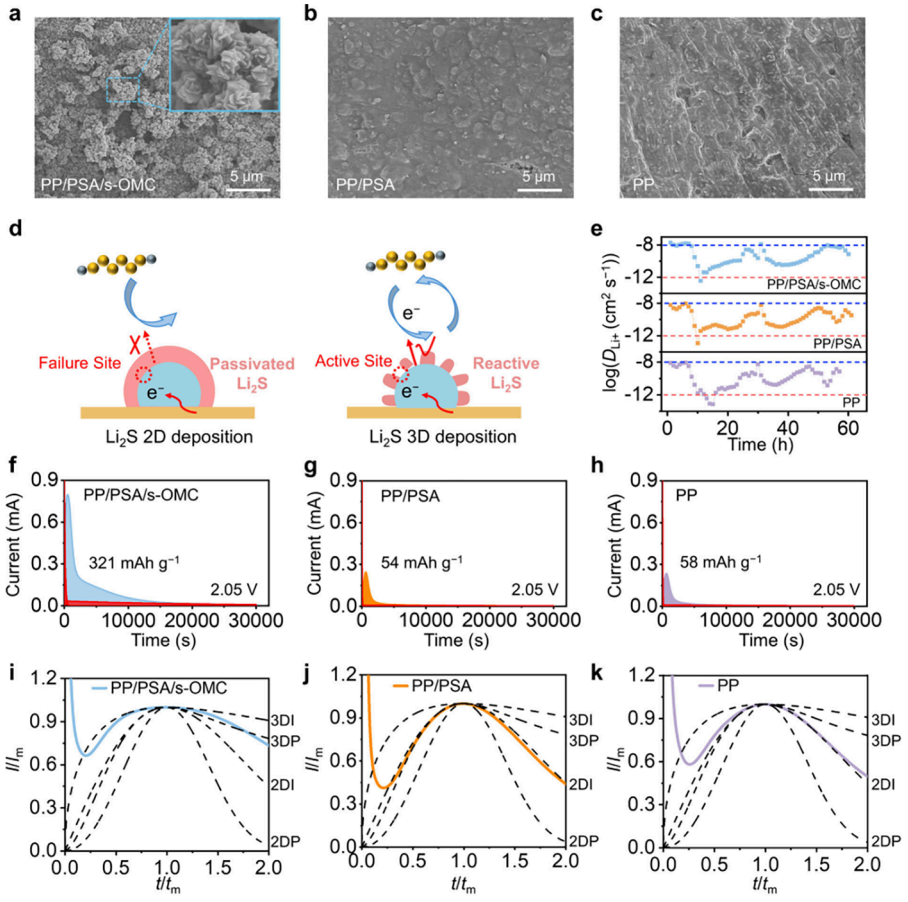

Figure 4. (a-c) SEM images showing the Li_2S deposition morphology of (a) PP/PSA/s-OMC, (b) PP/PSA, and (c) PP cells. (d) Schematic illustration of different deposition modes of Li_2S. (e) D_{Li^+} values obtained from GITT measurements. (f-h) Potentiostatic discharge profiles of Li-S cells with Li_2S_8 catholyte and different separators at 2.05 V. (i-k) Normalized chronoamperometric profiles depicting transient Li_2S nucleation and growth behaviors in different systems.

22.8° (Figure S9), corresponding to the (002) plane of graphitic microcrystallites. Raman spectroscopy reveals characteristic D and G bands at 1345 cm^{-1} and 1585 cm^{-1}, respectively (Figure S10). The interconnected sp^2-carbon domains can form a percolating conductive network in s-OMC. Therefore, the s-OMC layer not only aids ion transport but also acts as an electron mediator at the electrode interface, which mobilizes accumulated electrons and accelerates the electrode reaction kinetics.

To evaluate the interfacial compatibility of PSA, Li||Li symmetric cells were cycled at 1 mA cm^{-2} with a plating capacity of 1 mAh cm^{-2}. The cell with the PP separator exhibits a large initial voltage polarization of 110 mV and fails due to dendrite penetration after 130 h (Figure 2a, 2b). Postcycle SEM shows extensive inactive deposits on the lithium surface (Figure 2c). During cycling, lithium deposition generates localized stress. The PMMA with relatively low modulus exhibits inferior puncture resistance (Figure S11), making it a weaker physical barrier against dendrites compared to the PSA blend. The PP/PSA battery sustains stable cycling for over 800 h with minimal polarization (24 mV) and lower interfacial resistance (Figure S12). The improved battery performances are attributed to three factors: (1) The mechanical robustness of the PSA gel buffer layer enables effective dendrite suppression; (2) Polar ester groups in PSA facilitate the formation of a LiF-rich solid-electrolyte interphase (SEI) (Figure S13), promoting rapid Li^+ transport and mitigating concentration gradients; (3) The uniform PSA surface generates homogeneous Li^+ flux, yielding compact, dendrite-free lithium deposition (Figure 2d). The Tafel plots further confirm enhanced Li^+ transfer kinetics for batteries incorporating PSA (Figure S14). The Janus-structured PP/PSA/s-OMC separator induces spatially heterogeneous lithium deposition in symmetric batteries. On the PSA side facing the anode, uniform topography promotes compatible interfacial contact and planar deposition (Figure 2e). Conversely, the s-OMC side exhibits micrometer-scale roughness and localized charge accumulation (Figure 1b), creating current density hotspots that trigger preferential nucleation and dendritic growth (Figure 2f). This asymmetry feature is reflected in voltage profiles, with PSA maintaining stable overpotentials (~31 mV), while s-OMC shows irregular fluctuations (>47 mV) (Figure 2b). These results validate the critical role of the PSA gel buffer layer in stabilizing the lithium anode interface.

To understand how the Janus-structured separator improves sulfur redox kinetics, cyclic voltammetry (CV) tests of Li-S batteries were conducted. As shown in Figure 3a, the PP/PSA/s-OMC cell shows the highest peak currents and smallest polarization, indicating superior reaction kinetics and reversibility. Tafel analysis of the reduction (I) and oxidation (II) processes further confirms faster conversion kinetics for PP/PSA/s-OMC, yielding lower slopes of 62 and 83 mV dec^{-1}, respectively (Figure 3b). Electrochemical impedance spectra (EIS) results corroborate these findings, showing reduced

https://doi.org/10.1021/acs.nanolett.6c00616
Nano Lett. XXXX, XXX, XXX−XXX

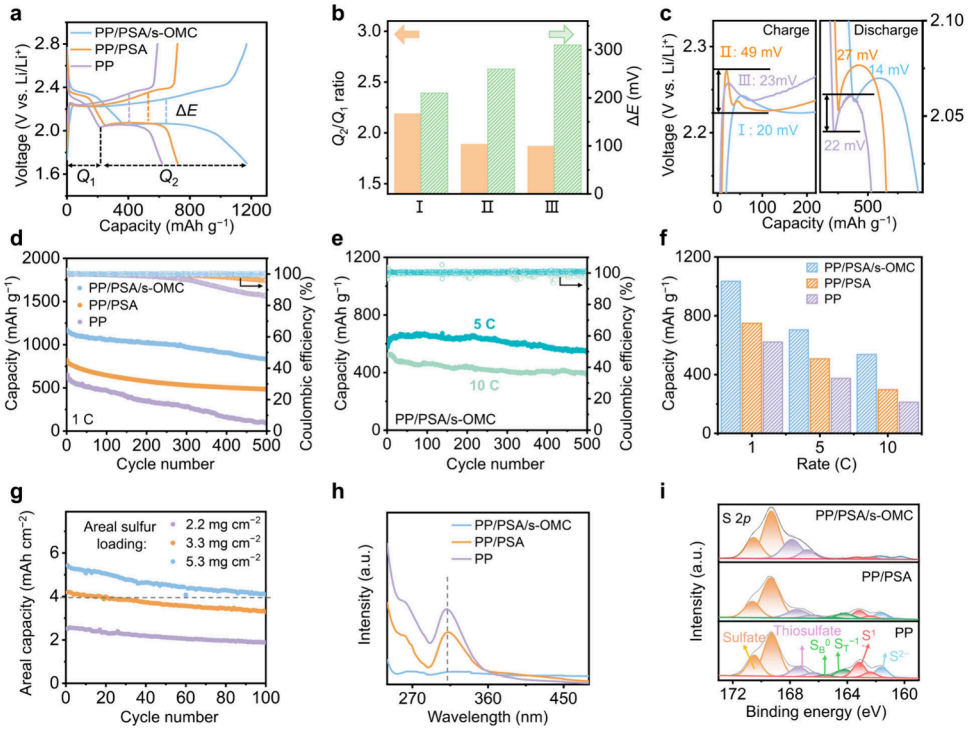

Figure 5. (a) Galvanostatic charge−discharge voltage profiles of Li-S batteries at 1 C. (b) Corresponding overpotential (ΔE) and capacity ratio (Q_2/Q_1) derived from panel (a). I is PP/PSA/s-OMC, II is PP/PSA, and III is PP. (c) Magnified view highlighting Li_2S nucleation during discharge and Li_2S activation during charging. (d) Cycling stability at 1 C. (e) High-rate cycling performance at 5 and 10 C for cells using the PP/PSA/s-OMC separator. (f) Discharge capacities versus current rates. (g) Cycling performance of Li-S batteries with PP/PSA/s-OMC separators and high sulfur loading cathodes. (h) UV−vis analysis of LiPS species in separator washing solutions from cycled cells. (i) XPS surface characterization of cycled lithium anodes.

charge-transfer resistance with s-OMC interlayer incorporation (Figure 3c). To quantitatively analyze the electrode reactions, CV tests were performed at different scan rates (Figures 3d-3f). By fitting the peak currents against the square root of the scan rates, the apparent lithium-ion diffusion coefficients (D_{Li^+}) of redox processes were calculated via the Randles−Sevcik equation (Figure 3g).[33] The PP/PSA/s-OMC cell achieves high D_{Li^+} values of 1.90×10^{-7}, 4.21×10^{-8}, and 6.29×10^{-8} $cm^2\ s^{-1}$ (Figure 3h), respectively, compared to PP (9.05×10^{-8}, 3.85×10^{-8}, and 4.20×10^{-8} $cm^2\ s^{-1}$). The increased D_{Li^+} of PP/PSA/s-OMC helps reduce concentration polarization at the electrode/electrolyte interface, thereby accelerating the conversion kinetics of sulfur species. Electrochemical performance was further investigated by comparing s-OMC with conductive carbon (Kejenblack, KB) as a control. The PP/PSA/s-KB cell shows lower D_{Li^+} values of 8.91×10^{-8}, 1.71×10^{-8}, and 3.68×10^{-8} $cm^2\ s^{-1}$, respectively (Figure S15). The s-KB particles exhibit higher tortuosity and less continuous pathways, resulting in greater ionic transport resistance, as reflected in the lower ionic conductivity of PP/PSA/s-KB (1.53 mS cm^{-1}, Figure S16). In contrast, the well-defined, interconnected mesopores of s-OMC provide low-tortuosity channels that facilitate rapid ion transport and optimize interfacial ion distribution.

H-cell experiments visually show that PP/PSA/s-OMC blocks LiPSs more effectively than the control samples (Figure S17). However, slight solute permeation indicates that adsorption alone is insufficient to completely prevent gradual LiPS accumulation under static or low-current conditions. Therefore, to effectively mitigate LiPS shuttling, the adsorption effect must be coupled with accelerated conversion kinetics. Li_2S_6 symmetric cell tests reveal the highest response currents and the lowest polarization in the PP/PSA/s-OMC cell (Figure 3i). This confirms that rapid conversion substantially reduces the concentration and lifetime of mobile LiPS intermediates in the electrolyte.

The morphology of the discharge products directly reflects how different separators regulate Li_2S deposition (Figure 4a-4c). Theoretically, Li_2S deposits via two modes (Figure 4d). 2D nucleation refers to lateral expansion controlled by lattice incorporation, which forms a dense passivating layer on the cathode surface. The passivating layer severely impedes reaction kinetics, limits sulfur utilization, and hinders subsequent oxidation due to poor electrical contact. In contrast, the 3D nucleation mode features vertical growth of Li_2S controlled by ion diffusion. Transforming the inherently sluggish 2D deposition to a 3D mode is paramount for practical high-energy-density Li-S batteries.[34−36] For the PP/PSA/s-OMC cell, an island-like Li_2S architecture composed of stacked nanosheets is observed (Figure 4a). This 3D morphology stems from the dual ion/electron-mediating function of the s-OMC. Its high conductivity enhances charge transfer across insulating Li_2S, while its ordered porous structure guides the vertical growth of the discharge products.[37] The resulting open morphology prevents complete surface passivation, maintains pathways for Li^+ transport, and promotes the continuous conversion of LiPSs. By comparison, cells assembled with PP/PSA and PP separators show dense, film-like Li_2S deposits (Figure 4b, 4c), indicative of the 2D nucleation mode. This compact layer acts as a kinetic barrier, hindering effective charge transfer and resulting in a limited discharge capacity.

https://doi.org/10.1021/acs.nanolett.6c00616
Nano Lett. XXXX, XXX, XXX−XXX

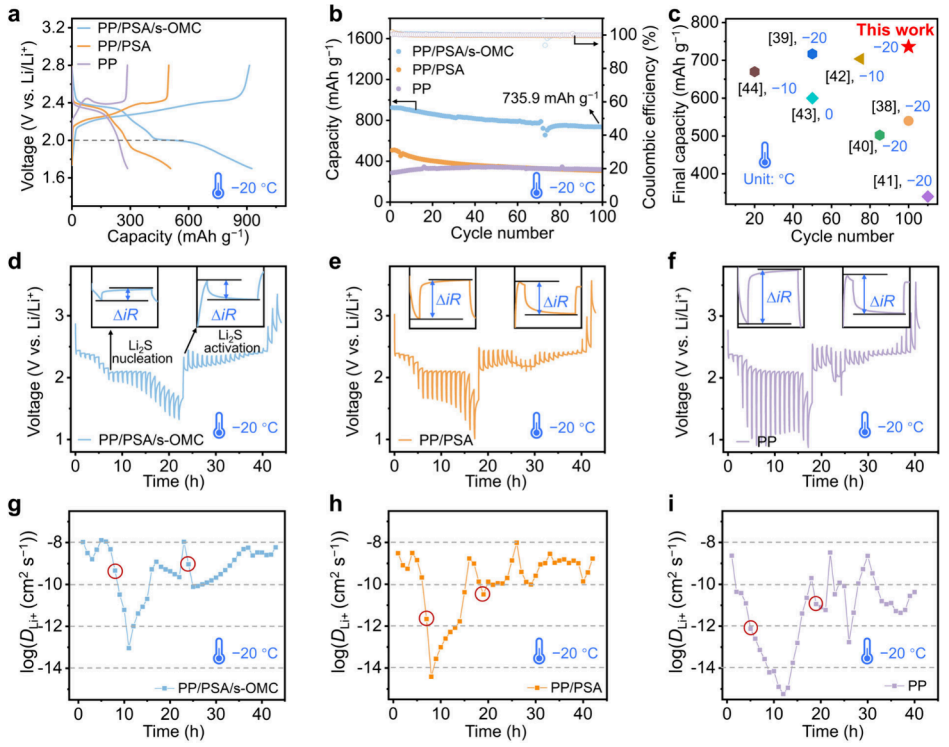

Figure 6. (a) Galvanostatic charge/discharge voltage profiles at −20 and 0.1 C. (b) Low-temperature cycling performance at −20 °C and 0.1 C. (c) Comparison of low-temperature performance against the state-of-the-art Li-S batteries. (d-f) GITT profiles of Li-S batteries at −20 °C. The insets magnify the instantaneous ohmic overpotential (ΔiR) at the key stages corresponding to Li_2S nucleation (~2.1 V) and Li_2S activation (~2.4 V). (g-i) The corresponding lithium-ion diffusion coefficients (D_{Li^+}) calculated from the GITT data.

The galvanostatic intermittent titration technique (GITT) was performed to quantify ion diffusion dynamics during multiphase transformations in Li-S chemistry. The depth of voltage dips in the discharge/charge curves (insets in Figure S18) reflects the instantaneous ohmic overpotential (ΔiR) associated with Li_2S nucleation and activation processes. Consistent with the CV-derived results, the PP/PSA/s-OMC battery exhibits the lowest polarization and the highest D_{Li^+} at the onset of Li_2S nucleation and activation (Figure 4e). To further characterize Li_2S deposition behavior, potentiostatic discharge tests and dimensionless chronoamperometric analysis were performed. The PP/PSA/s-OMC cell delivers a Li_2S deposition capacity of 321 mAh g^{-1} (Figure 4f), significantly higher than those of PP/PSA (54 mAh g^{-1}, Figure 4g) and PP (58 mAh g^{-1}, Figure 4h). Dimensionless chronoamperometric analysis confirms a 3D progressive (3DP) nucleation mode for PP/PSA/s-OMC (Figure 4i), whereas PP/PSA and PP exhibit 2D instantaneous (2DI) nucleation (Figure 4j, 4k). The conductive s-OMC interface promotes the radial growth of Li_2S by balancing surface atomic diffusion and mass transport in the electrolyte. This 3D deposition helps to maintain low interfacial impedance during cycling (Figure S19) and improves sulfur utilization.

Based on the 3D deposition of reactive Li_2S with accelerated conversion kinetics, the viability of PP/PSA/s-OMC separators in Li-S batteries under practical conditions (i.e., high current rates, high sulfur loadings, and low temperatures) was systematically investigated. As shown in Figure 5a, the PP/PSA/s-OMC battery delivers an initial discharge capacity of 1170 mAh g^{-1} at 1 C, significantly higher than those of PP/PSA (819 mAh g^{-1}) and PP (650 mAh g^{-1}) counterparts. Notably, the PP/PSA/s-OMC battery exhibits the highest capacity ratio (Q_2/Q_1 = 2.19) and lowest polarization potential (ΔE = 210 mV) (Figure 5b), confirming enhanced redox kinetics. Magnified charge/discharge voltage profiles further reveal the lowest overpotential during the Li_2S nucleation/activation processes (Figure 5c), demonstrating that Li_2S is more reactive at the cathode/electrolyte interface under the effect of a dual-ion/electron-conducting interfacial mediator. After 500 cycles at 1 C, the PP/PSA/s-OMC battery retains a discharge capacity of 871 mAh g^{-1} (capacity retention of 74.5%) and Coulombic efficiency exceeding 99.5% (Figure 5d and Figure S20). To demonstrate the role of s-OMC mediator as an interlayer, we also conducted comparative experiments by introducing an equivalent s-OMC mass directly into the cathode during slurry preparation (denoted as Sulfur/s-OMC cathode), paired with a PP/PSA separator (PP/PSA-Sulfur/s-OMC cell). The control configuration delivers a discharge capacity of 794 mAh g^{-1} at 1 C and maintains a capacity retention of 72.0% after 200 cycles (Figure S21). While the s-OMC as conductive additives in the cathode can modestly improve the sulfur utilization, they cannot spatially modulate ion/electron flux at the cathode/electrolyte interface or enable 3D Li_2S deposition. Consequently, the electrochemical performance of PP/PSA-Sulfur/s-OMC is inferior to that of PP/PSA/s-OMC.

High-rate cycling performance was evaluated at 5 and 10 C (Figure 5e, 5f). The PP/PSA/s-OMC battery exhibits capacities of 704 mAh g^{-1} (5 C) and 537 mAh g^{-1} (10 C), with Coulombic efficiencies of 99.5% and 99.0%, respectively. Even at 10 C, the charge−discharge profiles retain two distinct discharge voltage plateaus (Figure S22). In contrast, control cells exhibit severe polarization and capacity decline as the current density increases (Figure S23). Given that high sulfur

https://doi.org/10.1021/acs.nanolett.6c00616
Nano Lett. XXXX, XXX, XXX−XXX

loading exacerbates performance degradation in Li-S batteries, the practical viability of PP/PSA/s-OMC was assessed under more demanding conditions. The modified cell with 5.3 mg cm^{-2} sulfur loading exhibits a high areal capacity of 5.43 mAh cm^{-2} (Figure 5g), exceeding that of commercial Li-ion batteries (4 mAh cm^{-2}), and retained 75.9% of its initial capacity after 100 cycles. To probe the suppression of LiPSs shuttling, cycled separators and lithium anodes were analyzed. Ultraviolet−visible (UV−vis) spectra of the washing solution from the cycled PP/PSA/s-OMC separator showed no detectable sulfur species, whereas pronounced signals were observed for PP (Figure 5h). Post-mortem SEM characterizations revealed a smoother and more uniform lithium surface in cells with PP/PSA/s-OMC (Figure S24a-c), consistent with reduced interfacial side reactions and more uniform Li deposition. Energy-dispersive X-ray spectroscopy (EDS) and X-ray photoelectron spectroscopy (XPS) analyses showed significantly lower sulfur content on the lithium anode surface (Figure S24d-f, Figure 5i), confirming that the modified separator effectively mitigates the shuttle effect and contributes to enhanced electrochemical performances.

Owing to high ionic conductivity (0.85 mS cm^{-1} at −20 °C, Figure S25) and fast electrochemical kinetics, the PP/PSA/s-OMC cell operated under −20 °C delivers an initial discharge capacity of 922 mAh g^{-1} at 0.1 C and retains 737 mAh g^{-1} after 100 cycles, with well-defined voltage plateaus throughout cycling (Figure 6a, 6b). In contrast, the PP battery exhibits a much lower discharge capacity of 322 mAh g^{-1} and loses the second discharge plateau completely, indicating severe polarization and sluggish Li_2S deposition kinetics at low temperature. These results demonstrate that PP/PSA/s-OMC separator enables superior electrochemical performance under high sulfur loading and low temperature (−20 °C) (Figure 6c, Figure S26, Table S2, and Table S3).[25,38−48] Preventing LiPSs aggregation and accelerating the conversion of Li_2S_4 to solid Li_2S are key factors for stable operation at low temperatures.[34,49] As shown in the GITT data at −20 °C (Figure 6d-6f), the ohmic overpotential (ΔiR) for the PP/PSA/s-OMC cell is markedly smaller than that of the control cells during Li_2S deposition (~2.1 V). The calculated D_{Li^+} at the onset of Li_2S nucleation reaches 4.62×10^{-10} cm^2 s^{-1}, significantly outperforming the control cells (Figure 6g-6i, Table S4). As an efficient interfacial mediator, the dual-ion/electron-conducting s-OMC layer not only homogenizes Li^+ flux but also provides ample electron supply and active sites for the reduction of Li_2S_4. Similarly, during the initial charging stage (~2.4 V, corresponding to Li_2S oxidation activation), the PP/PSA/s-OMC cell exhibits small ohmic overpotential and high D_{Li^+} (9.25×10^{-10} cm^2 s^{-1}), outperforming the control cells. The 3D deposition maintains continuous pathways for electrons and ions, which are crucial for sustaining low ohmic impedance and supporting efficient redox reactions under demanding conditions.

In this work, we demonstrate a Janus-structured PP/PSA/s-OMC separator as both a charge-carrier transport vehicle and electron transfer mediator to steer Li_2S deposition into spatially controlled 3D pathways. This miscible blend PSA gel buffer layer uniformly wraps on the PP separator, reducing interfacial impedance for dendrite-free Li plating/stripping and acting as a gel-polymer buffer to prevent internal short circuits. The cathode-facing s-OMC layer functions as a dual-ion/electron-conducting interfacial mediator, thereby enhancing interfacial Li^+ diffusivity to accelerate redox kinetics and directing 3D nucleation/growth of Li_2S to avoid interfacial passivation and degradation. Consequently, the Janus PP/PSA/s-OMC separator enables exceptional Li-S battery performance under practical and challenging conditions, including stable cycling at high sulfur loading (5.43 mAh cm^{-2} at 5.3 mg cm^{-2}), high-rate capability (704 mAh g^{-1} at 5 C), and remarkable low-temperature operation (922 mAh g^{-1} at −20 °C). This interfacial engineering strategy provides insights for separator architectures targeting practical high-energy-density Li-S batteries.

■ ASSOCIATED CONTENT

Supporting Information

The Supporting Information is available free of charge at https://pubs.acs.org/doi/10.1021/acs.nanolett.6c00616.

Experimental section, including detailed materials, methods, and experimental procedures; FTIR, TGA, SEM characterizations of separators; Optimization of coating thickness and corresponding performance comparison; Nitrogen adsorption−desorption isotherm, pore-size distribution, XRD, and Raman analysis of s-OMC; Ionic conductivity of different separators; Cycling stability of Li||Li cell with PP/PMMA; EIS plots of Li||Li cells; XPS characterizations of cycled lithium anodes; Tafel curves; CV analysis of PP/PSA/s-KB cell; Polysulfide shuttle results; GITT profiles; EIS curves of Li-S batteries after cycling; Detailed galvanostatic charge/discharge performance; Postcycle SEM and EDS characterizations of lithium anodes; Tables comparing the low-temperature and high-sulfur-loading performances of Li-S batteries. (PDF)

■ AUTHOR INFORMATION

Corresponding Authors

Chao Lai − *School of Chemistry and Materials Science, Jiangsu Normal University, Xuzhou, Jiangsu 221116, P. R. China;* orcid.org/0000-0002-6021-6343; Email: laichao@jsnu.edu.cn

Zhong Jin − *State Key Laboratory of Coordination Chemistry, MOE Key Laboratory of Mesoscopic Chemistry, MOE Key Laboratory of High Performance Polymer Materials and Technology, Jiangsu Key Laboratory of Green Energy Catalysis and Intelligent Chemical Engineering, Suzhou Key Laboratory of Green Intelligent Manufacturing of New Energy Materials and Devices, Tianchang New Materials and Energy Technologies Research Center, Institute of Green Chemistry and Engineering, School of Chemistry and Chemical Engineering, Nanjing University, Nanjing, Jiangsu 210023, P. R. China;* orcid.org/0000-0001-8860-8579; Email: zhongjin@nju.edu.cn

Authors

Wen Yan − *School of Chemistry and Materials Science, Jiangsu Normal University, Xuzhou, Jiangsu 221116, P. R. China;* orcid.org/0000-0003-0718-0182

Xiaoyue Li − *School of Chemistry and Materials Science, Jiangsu Normal University, Xuzhou, Jiangsu 221116, P. R. China*

Peng Liu − *State Key Laboratory of Coordination Chemistry, MOE Key Laboratory of Mesoscopic Chemistry, MOE Key Laboratory of High Performance Polymer Materials and Technology, Jiangsu Key Laboratory of Green Energy*

https://doi.org/10.1021/acs.nanolett.6c00616
Nano Lett. XXXX, XXX, XXX−XXX

Catalysis and Intelligent Chemical Engineering, Suzhou Key Laboratory of Green Intelligent Manufacturing of New Energy Materials and Devices, Tianchang New Materials and Energy Technologies Research Center, Institute of Green Chemistry and Engineering, School of Chemistry and Chemical Engineering, Nanjing University, Nanjing, Jiangsu 210023, P. R. China

Chi Wang − *School of Chemistry and Materials Science, Jiangsu Normal University, Xuzhou, Jiangsu 221116, P. R. China*

Hanpei Liu − *School of Chemistry and Materials Science, Jiangsu Normal University, Xuzhou, Jiangsu 221116, P. R. China*

Complete contact information is available at: https://pubs.acs.org/10.1021/acs.nanolett.6c00616

Author Contributions

W. Y., C. L., and Z. J. conceived the research idea and designed the experiments. W. Y. and X. L. prepared all the samples. W. Y., X. L., P. L., C. W. and H. L. performed the structural characterizations, electrochemical tests, and mechanism study. W. Y. and X. L. analyzed the data and wrote the original manuscript. The manuscript was written and revised through contributions of all authors. All authors have given approval to the final version of the manuscript.

Notes

The authors declare no competing financial interest.

■ ACKNOWLEDGMENTS

The authors are grateful for the funding support from the National Natural Science Foundation of China (22209062, 22222902, 22479074, 22475096, 22561160129, U25A20628), the Equipment Pre-Research and Ministry of Education Joint Fund (8091B02052407), the Fundamental Research Program Key Project of Jiangsu Province (BK20253008), the Science and Technology Major Project of Jiangsu Province (BG2024013), the Scientific and Technological Achievements Transformation Special Fund of Jiangsu Province (BA2023037), the Academic Degree and Postgraduate Education Reforming Project of Jiangsu Province (JGKT24_C001), the Key Core Technology Open Competition Project of Suzhou City (SYG2024122), the Open Research Fund of Suzhou Laboratory (SZLAB-1308-2024-TS005), and the Chenzhou National Sustainable Development Agenda Innovation Demonstration Zone Provincial Special Project (2023sfq11).

■ REFERENCES

(1) Chen, Y.; Wang, T.; Tian, H.; et al. Advances in Lithium−Sulfur Batteries: From Academic Research to Commercial Viability. *Adv. Mater.* **2021**, *33* (29), No. 2003666.

(2) Li, Z.; Sami, I.; Yang, J.; et al. Lithiated metallic molybdenum disulfide nanosheets for high-performance lithium−sulfur batteries. *Nature Energy* **2023**, *8*, 84−93.

(3) Lv, S.; Ma, X.; Ke, S.; et al. Metal-Coordinated Covalent Organic Frameworks as Advanced Bifunctional Hosts for Both Sulfur Cathodes and Lithium Anodes in Lithium-Sulfur Batteries. *J. Am. Chem. Soc.* **2024**, *146* (13), 9385−9394.

(4) Qi, B.; Hong, X.; Jiang, Y.; et al. A Review on Engineering Design for Enhancing Interfacial Contact in Solid-State Lithium−Sulfur Batteries. *Nano-Micro Letters* **2024**, *16*, 71.

(5) Han, Z.; Li, S.; Wu, Y.; et al. Challenges and key parameters in exploring the cyclability limitation of practical lithium−sulfur batteries. *Journal of Materials Chemistry A* **2021**, *9*, 24215−24240.

(6) Shi, H.; Sun, W.; Cao, J. Challenges and Solutions for Lithium−Sulfur Batteries with Lean Electrolyte. *Adv. Funct. Mater.* **2023**, *33* (42), No. 2306933.

(7) Yan, W.; Wei, J.; Chen, T.; et al. Superstretchable, thermostable and ultrahigh-loading lithium-sulfur batteries based on nanostructural gel cathodes and gel electrolytes. *Nano Energy* **2021**, *80*, No. 105510.

(8) Zhao, Q.; Zhu, Q.; Liu, Y.; et al. Status and prospects of MXene-based lithium-sulfur batteries. *Adv. Funct. Mater.* **2021**, *31* (21), No. 2100457.

(9) Lin, Y.; Li, L.; Tan, L.; et al. Accelerating lithium-sulfur battery reaction kinetics and inducing 3D deposition of Li_2S using interactions between Fe_3Se_4 and lithium polysulfides. *Journal of Energy Chemistry* **2024**, *95*, 540−553.

(10) Yan, W.; Yan, K. Y.; Kuang, G. C.; et al. Fluorinated quinone derived organosulfur copolymer cathodes for long-cycling, thermostable and flexible lithium-sulfur batteries. *Chemical Engineering Journal* **2021**, *424*, No. 130316.

(11) Waqas, M.; Niu, Y.; Tang, M.; et al. A decade of development in cathode-facing surface modified separators for high-performance Li-S batteries. *Energy Storage Materials* **2024**, *72*, No. 103682.

(12) Huang, Y.; Lin, L.; Zhang, C.; et al. Recent advances and strategies toward polysulfides shuttle inhibition for high-performance Li-S batteries. *Advanced Science* **2022**, *9* (12), No. 2106004.

(13) Xie, J.; Cheng, F.; Chen, R.; et al. Promoting overall sulfur redox kinetics for Li-S batteries via interfacial synergy in a NiS-$NiTe_2$ heterostructure-modified separator. *Journal of Materials Chemistry A* **2024**, *12* (18), 10737−10744.

(14) Tian, S.; Zeng, Q.; Liu, G.; et al. Multi-dimensional composite frame as bifunctional catalytic medium for ultra-fast charging lithium-sulfur battery. *Nano-Micro Letters* **2022**, *14* (1), 196.

(15) Han, Z.; Ren, H.; Huang, Z.; et al. A Permselective Coating Protects Lithium Anode toward a Practical Lithium−Sulfur Battery. *ACS Nano* **2023**, *17* (5), 4453−4462.

(16) Jiang, Y.; Hong, X.; Huang, P.; et al. Interfacial fusion-enhanced 11 μm-thick gel polymer electrolyte for high-performance lithium metal batteries. *Journal of Energy Chemistry* **2024**, *98*, 58−66.

(17) Xia, S.; Zhang, X.; Liang, C.; et al. Stabilized lithium metal anode by an efficient coating for high-performance Li−S batteries. *Energy Storage Materials* **2020**, *24*, 329−335.

(18) Song, X.; Liang, X.; Eko, J. Toward Practical Li−S Batteries: On the Road to a New Electrolyte. *Adv. Funct. Mater.* **2024**, *14* (46), No. 2402506.

(19) Zhong, Y.; Huang, P.; Yan, W.; et al. Ion-conductive polytitanosiloxane networks enable a robust solid-electrolyte interface for long-cycling lithium metal anodes. *Adv. Funct. Mater.* **2022**, *32*, No. 2110347.

(20) Shi, Z.; Tian, Z.; Guo, D. Kinetically Favorable Li−S Battery Electrolytes. *ACS Energy Letters* **2023**, *8* (7), 3054−3080.

(21) Jin, W.; Guo, Y.; Gan, T.; et al. Cooperation of Multifunctional Redox Mediator and Separator Modification to Enhance Li-S Batteries Performance under Low Electrolyte/Sulfur Ratio. *Angew. Chem., Int. Ed.* **2025**, *64* (8), No. e202420544.

(22) Wu, Z.; Liu, M.; He, W.; et al. Unveiling the autocatalytic growth of Li_2S crystals at the solid-liquid interface in lithium-sulfur batteries. *Nat. Commun.* **2024**, *15*, 9535.

(23) Li, F.; Zhou, G.; Pei, S.; et al. A graphene-pure-sulfur sandwich structure for ultrafast, long-life lithium-sulfur batteries. *Adv. Mater.* **2014**, *26* (4), 625−631.

(24) Zhu, S.; Gong, L.; Pan, Y.; et al. Coral-like interconnected carbon aerogel modified separator for advanced lithium-sulfur batteries. *Electrochim. Acta* **2020**, *354*, No. 136637.

(25) Kong, Y.; Qiu, X.; Xue, Y.; et al. Sulfonic Acid-Functionalized Graphdiyne for Effective Li-S Battery Separators. *J. Am. Chem. Soc.* **2024**, *146* (34), 23764−23774.

(26) Zheng, Y.; Yi, Y.; Fan, M.; et al. A high-entropy metal oxide as chemical anchor of polysulfide for lithium-sulfur batteries. *Energy Storage Materials* **2019**, *23*, 678−683.
(27) Huang, J.; Zhang, Q.; Peng, H.; et al. Ionic shield for polysulfides towards highly-stable lithium−sulfur batteries. *Energy Environ. Sci.* **2014**, *7*, 347−353.
(28) Li, Y.; Wang, Z.; Gu, H. F.; et al. Niobium boride/graphene directing high-performance lithium-sulfur batteries derived from favorable surface passivation. *ACS Nano* **2024**, *18* (12), 8863−8875.
(29) Deng, D. R.; Xiong, H. J.; Luo, Y. L.; et al. Accelerating the Rate-Determining Steps of Sulfur Conversion Reaction for Lithium-Sulfur Batteries Working at an Ultrawide Temperature Range. *Adv. Mater.* **2024**, *36* (39), No. 2406135.
(30) Ding, H.; Chen, Z.; Li, H.; et al. Regulating Li_2S Deposition and Accelerating Conversion Kinetics through Intracavity ZnS toward Low-Temperature Lithium-Sulfur Batteries. *Nano Lett.* **2024**, *24* (47), 15118−15126.
(31) Yang, B.; Yang, Y.; Xu, X.; et al. Hierarchical microstructure and performance of PVDF/PMMA/SiO_2 lithium battery separator fabricated by thermally-induced phase separation (TIPS). *J. Mater. Sci.* **2022**, *57*, 11274−11288.
(32) Zhao, L.; Wu, Z.; Wang, Z.; et al. Regulating Solvation Structures Enabled by the Mesoporous Material MCM-41 for Rechargeable Lithium Metal Batteries. *ACS Nano* **2022**, *16* (12), 20891−20901.
(33) Yan, W.; Yu, F.; Jiang, Y.; et al. Self-Assembly Construction of Carbon Nanotube Network-Threaded Tetrathiafulvalene-Bridging Covalent Organic Framework Composite Anodes for High-Performance Hybrid Lithium-Ion Capacitors. *Small structures* **2022**, *3*, No. 2200126.
(34) Chen, Z. X.; Zhang, Y. T.; Bi, C. X.; et al. Premature deposition of lithium polysulfide in lithium-sulfur batteries. *Journal of Energy Chemistry* **2023**, *82*, 507−512.
(35) Wang, B.; Wang, L.; Zhang, B.; et al. Niobium diboride nanoparticles accelerating polysulfide conversion and directing Li_2S nucleation enabled high areal capacity lithium-sulfur batteries. *ACS Nano* **2022**, *16* (3), 4947−4960.
(36) Fan, F. Y.; Carter, W. C.; Chiang, Y. M. Mechanism and Kinetics of Li_2S Precipitation in Lithium-Sulfur Batteries. *Adv. Mater.* **2015**, *27* (35), 5203−5209.
(37) Sun, J.; Liu, Y.; Liu, L.; et al. Interface engineering toward expedited Li_2S deposition in lithium-sulfur batteries: a critical review. *Adv. Mater.* **2023**, *35* (29), No. 2211168.
(38) Zhao, W.; Zhang, Y.; Liu, Q.; et al. Entropy-Modulated Short-Chain Cathode for Low-Temperature All-Solid-State Li−S Batteries. *Angew. Chem., Int. Ed.* **2025**, *64* (1), No. e202413670.
(39) Zhang, J. H.; Fan, X. Z.; Zhou, X. H.; et al. Charging lithium polysulfides by cationic lithium nitrate species for low-temperature lithium−sulfur batteries. *Energy Storage Materials* **2024**, *73*, No. 103786.
(40) Shi, J.; Yu, C.; Ning, Y.; et al. Strategic design of high-directional scaffold enabling accelerated kinetics for high-loading low-temperature lithium−sulfur batteries. *Chemical Engineering Journal* **2025**, *511*, No. 161939.
(41) Guo, D.; Thomas, S.; El-Demellawi, J. K.; et al. Electrolyte engineering for thermally stable Li−S batteries operating from − 20 to 100 °C. *Energy&Environmental Science* **2024**, *17* (21), 8151−8161.
(42) Zhang, J.; Chou, J.; Luo, X. X.; et al. A Fully Amorphous, Dynamic Cross-Linked Polymer Electrolyte for Lithium−Sulfur Batteries Operating at Subzero-Temperatures. *Angew. Chem., Int. Ed.* **2024**, *63* (5), No. e202316087.
(43) Wang, Z.; Ji, H.; Zhou, L. All-Liquid-Phase Reaction Mechanism Enabling Cryogenic Li−S Batteries. *ACS Nano* **2021**, *15* (8), 13847−13856.
(44) Li, Y.; Sun, K.; Fu, Y.; et al. ″Bowling Collision Effect" of $CoMo_6$ Polyoxometalate Units Enables Wide Temperature Range from − 20 to 60 °C and Dendrite Mitigation Li−S Batteries. *Adv. Mater.* **2024**, *36* (38), No. 2406343.
(45) Liu, L.; Zheng, Y.; Sun, Y.; et al. Modulation of Potential-Limiting Steps in Lithium-Sulfur Batteries by Catalyst Synergy. *Small* **2024**, *20* (25), No. 2309582.
(46) Liu, L.; Yan, M.; Zhao, X.; et al. A novel pathway for sustained sulfides conversion via electrocatalyst-modified separator in lithium-sulfur batteries. *Nano Energy* **2024**, *130*, No. 110122.
(47) Yeom, S.; Jo, H.; Lee, H.; et al. Lithiating cathodes for Li-S batteries: Regulating Li_2S electrodeposition to enhance sulfur utilization. *Energy Storage Materials* **2024**, *71*, No. 103644.
(48) Li, C.; Liu, X.; Zhu, L.; et al. Conductive and Polar Titanium Boride as a Sulfur Host for Advanced Lithium−Sulfur Batteries. *Chem. Mater.* **2018**, *30* (20), 6969−6977.
(49) Gupta, A.; Bhargav, A.; Jones, J.; Bugga, R.; Manthiram, A. Influence of Lithium Polysulfide Clustering on the Kinetics of Electrochemical Conversion in Lithium−Sulfur Batteries. *Chem. Mater.* **2020**, *32* (5), 2070−2077.

https://doi.org/10.1021/acs.nanolett.6c00616
Nano Lett. XXXX, XXX, XXX−XXX